Quasi-Fixed Points and Periodic Orbits in the Zebiak–Cane ENSO Model with Applications in Kalman Filtering. Part I: Monthly Quasi-Fixed Points

GERD BÜRGER, STEPHEN E. ZEBIAK, AND MARK A. CANE

Lamont-Doherty Earth Observatory, Columbia University, Palisades, New York

(Manuscript received 18 August 1994, in final form 21 February 1995)

ABSTRACT

In an effort to apply the interactive Kalman filter to higher-dimensional systems, the concept of a quasi-fixed point is introduced. This is defined to be a system state where the tendency, in a suitable reduced space, is at a minimum. It allows one to use conventional search algorithms for the detection of quasi-fixed points. In Part I quasi-fixed points of the ENSO model of Zebiak and Cane are found when run in a permanent monthly mode, the reduced space being defined via a multiple EOF projection. The stability characteristics of the quasi-fixed points are analyzed, and it is shown that they are significantly different from the (in)stabilities of the average monthly models. With these quasi-fixed points, assimilation experiments are carried out with the interactive Kalman filter for the Zebiak–Cane model in the reduced space. It is demonstrated that the results are superior to both a seasonal Kalman filter and the extended Kalman filter.

1. Introduction

In a recent study, Bürger and Cane (1994, henceforth BC) have shown that the assimilation of data into highly nonlinear systems via the extended Kalman filter (EKF) might fail and can successfully be remedied by what they call the "interactive Kalman filter" (IKF). If the system which is to be assimilated tends to occupy certain regimes, then, as the paper demonstrates, the continuous updating of the EKF assimilation error model can be replaced by a procedure that uses only the single regime error models. The filter works in such a way that all regimes participate in each assimilation step, the conflicting error models being reconciled through a weighting procedure that reflects the "closeness" of the system to the individual regimes at a specified time.

For an application of the IKF it is therefore crucial to know in advance which regimes to choose. In higher-dimensional (nonlinear) systems, it is usually near fixed points that the local structure of the system is richest, and the splitting of the full system into a group of corresponding localizations is very effective. Bürger and Cane deal with the one-dimensional double-well system and the three-dimensional Lorenz system. These systems are mathematically simple enough to calculate the various fixed points algebraically, but the situation quickly changes with increasing number of dimensions and becomes algebraically intractable for most models usually encountered in atmosphere–ocean studies.

The importance of fixed points for the understanding of atmospheric phenomena such as weather regimes has been boosted by the work of Charney and DeVore (1979) on multiple equilibria, that is, fixed points, of the barotropic potential vorticity equation on the beta plane. Since then much effort has been put in extending our knowledge about the spatial and temporal structure of such equilibria, and search methods for equilibria have been developed. Legras and Ghil (1985) determine zonal and blocking states of the atmospheric flow in two different ways: as stationary solutions of the barotropic potential vorticity equation on the sphere on the one hand, and as persistent anomalies of a corresponding model run on the other hand. Another approach has been undertaken by Branstator and Opsteegh (1989); they apply a numerical search algorithm for the minima of the tendency function. As a result, they find blocking structures very much like the persistent anomalies.

At a first glance, the atmosphere–ocean system of the tropical Pacific with the El Niño–Southern Oscillation (ENSO) phenomenon does not seem to fit into this picture: there is no evidence of a fixed point in the dynamics of that process, nor has anybody ever detected with certainty *regimes,* in the aforementioned sense, in the ENSO phenomenon. Nevertheless, in our study we show how one can successfully apply the interactive Kalman filter even to phenomena such as ENSO. The two facts, 1) that there are no fixed points

* Current affiliation: Potsdam Institut für Klimafolgenforschung, Potsdam, Germany.

Corresponding author address: Dr. Gerd Bürger, Potsdam Institut für Klimafolgenforschung e.V., Postfach 60 12 03, 14412 Potsdam, Germany.

in the system and 2) that it does not exhibit regimelike behavior, are mainly caused by the external forcing that is annually cyclic (through the radiation or, for an anomaly model, the seasonal cycle). We show that it is possible to reasonably extend the concept of a fixed point in two different directions that make it applicable to such systems. As a model of the tropical atmosphere–ocean system of the Pacific, we use the anomaly model of Zebiak and Cane (1987, henceforth denoted by ZC). The first direction, which will be the content of Part I, is to break up the nonautonomous (i.e., time dependent) model ZC into autonomous (i.e., time independent) pieces ZC_m, where the background mean fields that drive ZC are frozen to the conditions of a particular month m, and to consider fixed points of each ZC_m. The second approach (Part II, Bürger et al. 1995) is to consider the Poincare map imposed by the annual forcing and consider its fixed points. They form the initial points of periodic orbits of ZC.

For both approaches we need to define a notion that is slightly weaker than the notion of fixed point. It is implicitly in the above mentioned and other papers but has never received enough attention to be given a specific name, probably because of its proximity to the notion of fixed point. We decide to do otherwise and call it a *quasi-fixed point* (QFP), a name that indicates it is a straightforward generalization of a fixed point. At a QFP the absolute value of the tendency function assumes a local minimum, as opposed to zero for a true fixed point. Although QFPs always exist (except in some trivial cases), their detection requires a limited number of degrees of freedom. We therefore restrict the defining criterion for QFPs to certain low-dimensional subspaces of the full system space, where the subspace has to contain the information for all prognostic variables of ZC. This guaranteed, one can formally define a version M of the full system ZC, which exists in the low-dimensional subspace, and one can work exclusively with this version. Moreover, M should converge to ZC in the same way as the total space is approximated by the subspace. This means that important dynamical features of ZC, such as fixed points, limit cycles, bifurcations, and the like, should be reflected in M and can be detected there.

Although QFPs might be of limited importance in a theoretical sense, mainly because of the difficulties to define an appropriate subspace, they are nonetheless useful for applications of the IKF. With a series of Kalman filter studies for ZC (or M, respectively), we will demonstrate that the QFPs we found can successfully be used for the IKF. We compare the assimilation results with two other Kalman filters, a seasonal filter and the extended Kalman filter, and find that the IKF in all test cases performs better.

2. The projection

The model ZC couples a Gill-type atmospheric model with a 1.5-layer oceanic model; it describes and predicts anomalies that evolve around some empirically given climatological cycle. It has been demonstrated that usefully skillful predictions of ENSO at one year lead time are possible with ZC (cf. Cane et al. 1986; Latif et al. 1994). Model ZC is defined on a grid that covers the tropical pacific region between about 30°S and 30°N, and 120°E and 80°W, with a grid size of 2°–5° in longitude and 0.5°–2° in latitude, depending on the field variable. The time step of the model is one-third of a month. Table 1 shows the variables that define a *state* of ZC: given a certain time of the year, the evolution of ZC is uniquely determined by these variables.

We now define a multiple EOF projection for ZC in two steps. In the first step we calculate primary EOFs for each single variable from a 1000-month run of ZC and keep as many principal components (PCs) as account for 99% of the field variability (Table 1, right column). Before we can apply a secondary EOF projection to these PCs, we have to ensure that they are weighted according to their number and physical importance. As indicated in Table 1, we have four groups of variables: 1) the atmospheric part, 2) the atmospheric impact on the ocean, 3) the oceanic part, and 4) the oceanic impact on the atmosphere. We want each of these groups to be treated equally as a whole. As a result, the PCs in each group were weighted such that, first, in each single group all variables account for the same total variability and, second, all groups have equal total variability. The resulting 383-dimensional, mixed PC time series was then subject to another, secondary, EOF projection. Figure 1 depicts the first 20 eigenvalues of that EOF calculation and the two leading EOFs in their wind, thermocline (TCL), and SST fields; they explain about 65% of the full variance. The remaining EOFs taper off rather quickly to negligible values. Note that EOFs 1 and 2 do not seem to be in quadrature, which would have to be the case if the three fields were the only ones used for the EOF calculation. This is a hint toward the non–self-adjoint nature of ZC.

TABLE 1. State variables of ZC.

Variable	Description	No. of points	No. of PCs
u	zonal wind	34 × 30	13
v	meridional wind	34 × 30	17
$\nabla\cdot(u, v)$	wind divergence	34 × 30	44
τ	wind stress	34 × 30	23
H_R	Rossby part of thermocline	117 × 85	46
U_R	Rossby part U	117 × 85	74
V	meridional current	117 × 85	90
A_K	Kelvin wave amplitude	85	4
H_0	TCL at boundary	117 × 4	14
U_0	boundary zonal current	117 × 4	15
SST	sea surface temperature	34 × 30	29
Q	atmospheric heating	34 × 30	14
	Total:	37 996	383

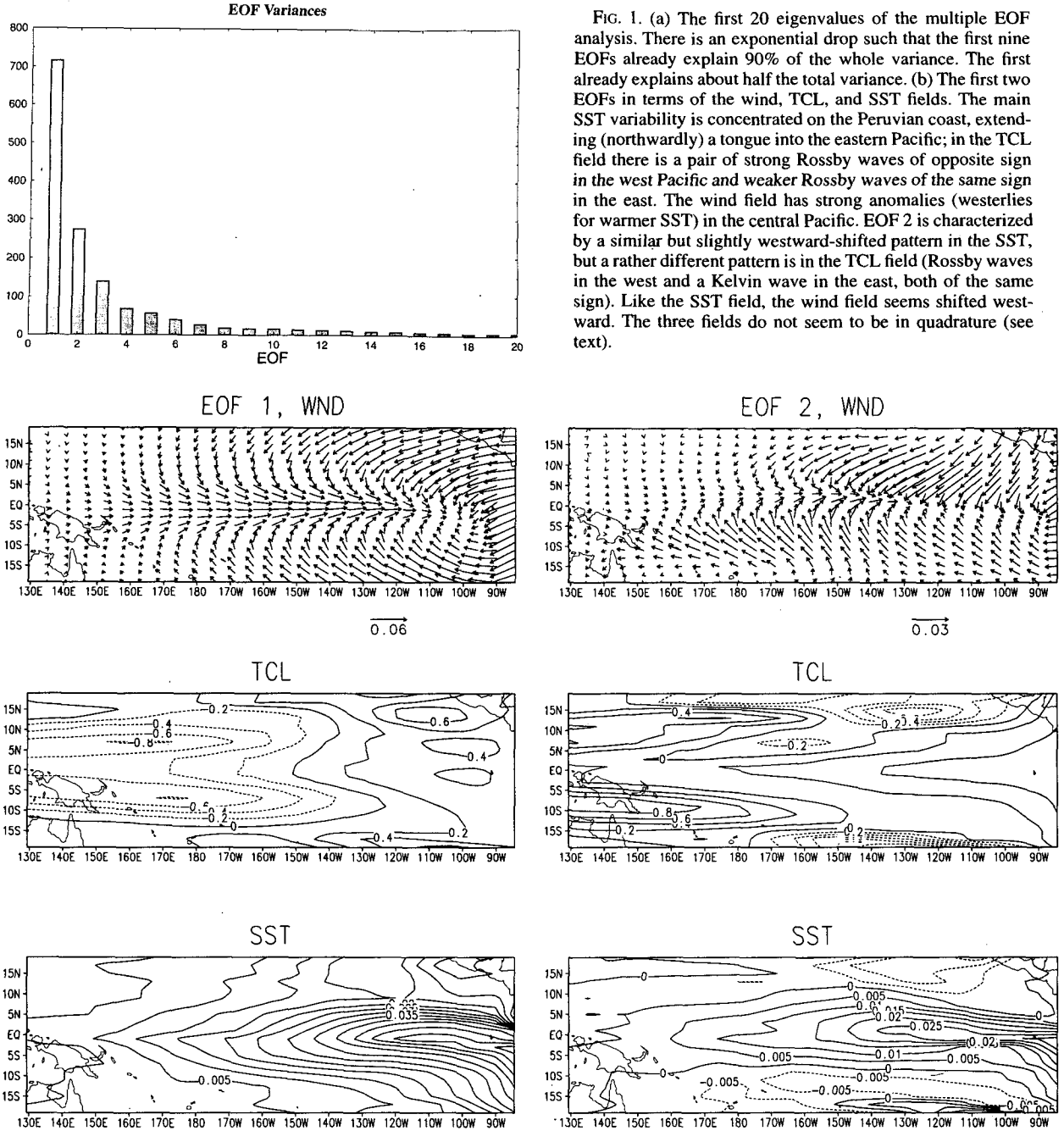

FIG. 1. (a) The first 20 eigenvalues of the multiple EOF analysis. There is an exponential drop such that the first nine EOFs already explain 90% of the whole variance. The first already explains about half the total variance. (b) The first two EOFs in terms of the wind, TCL, and SST fields. The main SST variability is concentrated on the Peruvian coast, extending (northwardly) a tongue into the eastern Pacific; in the TCL field there is a pair of strong Rossby waves of opposite sign in the west Pacific and weaker Rossby waves of the same sign in the east. The wind field has strong anomalies (westerlies for warmer SST) in the central Pacific. EOF 2 is characterized by a similar but slightly westward-shifted pattern in the SST, but a rather different pattern is in the TCL field (Rossby waves in the west and a Kelvin wave in the east, both of the same sign). Like the SST field, the wind field seems shifted westward. The three fields do not seem to be in quadrature (see text).

The question of which of these EOFs are physically significant is as important since it is always subject of much speculation [see, e.g., Preisendorfer (1988), who gives a full palette of selection rules together with the context where each rule should be applied]. But here we adopt the viewpoint that there is just no clear-cut difference between the *signal* and the *noise* of the above process. We decided to keep 90% of the variance, and in the following we might refer to that portion as the "signal" and to the rest as the "noise."

Formally, the twofold projection can be described as follows. We denote the ZC state vector by

$$\mathbf{z} = [u, v, \nabla\cdot(u, v), \tau, H_R, U_R, V, A_K, H_0, U_0, T, Q] \quad (1)$$

and the principal components of the secondary EOF projection by $\mathbf{x}$. Now we comprise the primary EOFs to a single 37 996 × 383 matrix $\mathbf{E}_1$. Here $\mathbf{E}_1$ is a diagonal matrix, the entries of which are rectangular matrices consisting of the primary EOFs. The nine leading

secondary EOFs explain 90% of the variance of the secondary PCs; we represent them in a 383 × 9 matrix, $\mathbf{E}_2$. Forming the diagonal (383 × 383) matrix $\mathbf{\Lambda}$, which consists of the different weightings of the primary principal components, we can write the projection as

$$x = \mathbf{E}_2^{\mathrm{T}} \mathbf{\Lambda} \mathbf{E}_1^{\mathrm{T}} \mathbf{z}. \tag{2a}$$

The orthogonality of the EOFs ensures that the embedding

$$\mathbf{z} = \mathbf{E}_1 \mathbf{\Lambda}^{-1} \mathbf{E}_2 \mathbf{x} \tag{2b}$$

is inverse to the projection (2a), so that the multiple EOF reduction works like a simple one.

3. Quasi-fixed points

Equation (2) ensures that it is possible to pull every map in the full space down to the EOF space. When we apply this to the map that assigns to each state $\mathbf{z}$ the state $\mathbf{z}'$ that originates from $\mathbf{z}$ by advancing ZC_m by one time step, we arrive at the following diagram.

$$\begin{array}{ccc} & \overset{ZC_m}{\longrightarrow} & \\ z & & z' \\ \text{embedding} \Uparrow & & \Downarrow \text{projection} \\ x & & x' \\ & \underset{M_m}{\longrightarrow} & \end{array}$$

As the diagram emphasizes, there is a unique model (function), M_m, that assigns to any $\mathbf{x}$ in the EOF space a new value $\mathbf{x}'$ and that by definition can be considered as a projected version of ZC_m. With increasing resolution of the EOF subspace, one can expect that M_m, as far as short time behavior is concerned, converges to ZC_m, just as the eigenvalues in Fig. 1 converge to zero. Hence, as soon as the EOF projection extends to the realm of noise, M_m should faithfully reflect the main dynamical features of ZC_m, especially fixed points and their stability structures.

For a fixed-point x of M_m one has $M_m(x) = x$ or $M_m(x) - x = 0$. Therefore, any fixed point is a root of the nonnegative real-valued function

$$\Gamma(x) = |M_m(x) - x|. \tag{3}$$

We define a QFP of M_m to be a local minimum of Γ. For a QFP x, the smaller $\Gamma(x)$ the closer x is to a true fixed point (of M_m). Although a QFP depends on the particular EOF truncation, we sometimes speak of a QFP of ZC_m, for example, referring to an imaginary "ideal" projection that perfectly filters out the noise of the system. In this case, the existence of a QFP x with a negligible value of Γ has another interesting aspect: either x is a fixed point of ZC_m or ZC_m maps x directly toward higher EOFs, which in our case means noise. In either case x is a pivotal point in the model's local error structure, and it can help assimilation error models to adjust their behavior effectively. Unlike fixed points, QFP always exist in a nontrivial system. Furthermore, there is a straightforward way to estimate them, as described next.

4. Estimation of quasi-fixed points for ZC_m

To estimate the average variability of the model, we conducted one long run of ZC_7 (i.e., in the perpetual July mode) over 3600 model time steps (= 100 years). Figure 2 depicts the function

$$\hat{\Gamma}(t) = |x(t+1) - x(t)|, \tag{4}$$

where each $x(t)$ is the projection of the current state of ZC_m. Here $\hat{\Gamma}(t)$ is a good approximate of $\Gamma[x(t)]$, depending on the quality of the EOF projection. Note the broad range of values that sometimes approach zero (years 40–50) and sometimes exceed 15 (first 20 years). We see that during the first 30 years the model behaves very regularly, performing about seven cycles of period 30/7 ~ 4.3 years. In this period the typical $\hat{\Gamma}(t)$ values are close to 5, but sporadically they can reach maximum values. The next 10–15 years seem locked at the state of no anomalies [with zero $\hat{\Gamma}(t)$ values, of course], but then the system slowly begins to oscillate again, finally assuming a behavior that looks more chaotic than the beginning, with $\hat{\Gamma}(t)$ values that lie somewhat lower, in the range 1–10. [Compare this figure to Fig. 10 of Legras and Ghil (1985), which shows the corresponding tendency function for their model.]

Term Γ^2 is a sum of quadratic functions. Local minima of such functions can be estimated with the Marquart–Levenberg technique (code libraries such as minpack or IMSL contain appropriate routines). Because these routines calculate the Jacobian of Γ, $\nabla\Gamma$, internally we merely have to provide a subroutine that calculates Γ from a given input vector and a starting

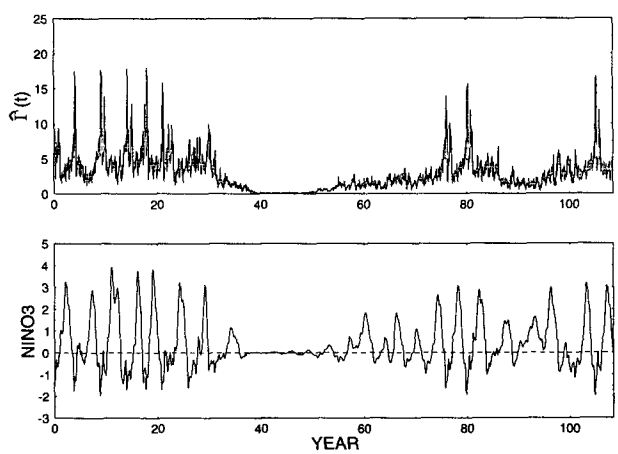

FIG. 2. A section of the permanent July run ZC_7, showing the NINO3 values in the lower panel and, in the other panel, the function $\Gamma(t)$, which measures the absolute tendency (in the EOF phase space) of the model. The largest values occur when the model exhibits a regular cycle of about a 4.3-yr period, reaching values of up to 17. Here the average value of about five is also higher than at the end of the time series when the oscillation is not so regular; here the average tendency is no greater than two or three. We can see that the large spikes are associated with a sharp change in the NINO3 during the cold phase.

point. For a fuller description of the procedure compare Press et al. (1992). We therefore merely have to translate the steps depicted in the diagram (4) into programming code. We definitely do not want to describe the details of this work but we have to remark on this: because the code needs a lot of cross, back, and forth references, it is quite difficult to define what can be called a *unique state of the system.* This, however, is necessary for the definition of a *function.* The need to work in a reduced space becomes especially clear when we note that the calculation of $\nabla\Gamma$ alone would require 37 996 model steps and the result, which is a 37 996 $\times$ 37 996 matrix, that is, 1 Gbyte of numbers, has to be stored in memory.

As mentioned in the beginning, we wanted to keep 90% of the model variance and therefore retained the nine leading multiple EOFs. The starting points for the search algorithm were generated by a random process with covariance $C = C_9$, which is the covariance of the nine corresponding PCs. We used 50 different points for each month. A major problem in the search algorithm arises from the fact that the state of no anomalies is a fixed point for all months. It turned out that if the limitation criterion of the search algorithm was chosen too strict, the algorithm was only attracted by this fixed point. Therefore, if one wants to gain a thorough picture of the whole state space and its QFPs, one has to soften the limitation criterion and use the outcome of a search procedure as input for a new search, and so on. This needs a lot of tuning and trying and, especially, a great number of iterations. Finally, the search iteration converged to five groups of states, where each group represented the individual shaping for each month of an otherwise generic pattern. It is justified, hence, to refer to each single group as *one* QFP that undergoes slight modifications through the year. We denote these QFPs as QFP 1, $\cdots$, QFP 5, ordered by increasing NINO3 values. QFP 3 is the state of zero anomalies, a fixed point for each month m.

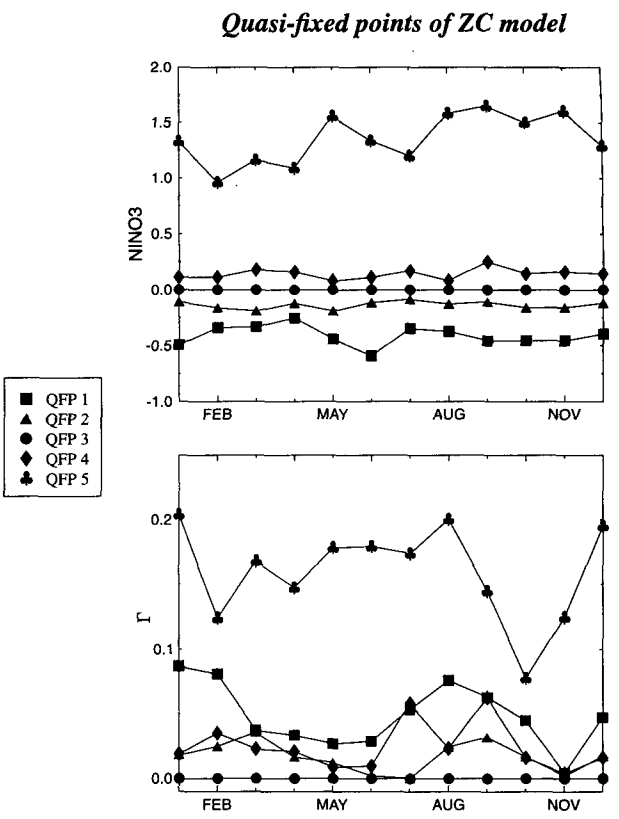

FIG. 3. The quasi-fixed points of the models ZC_m, $m = 1, \ldots, 12$. In the lower panel we see the value of Γ for each QFP. With the exception of QFP 5 (and partly QFP 1), all values are well below 0.1; this is about one-tenth of the usual tendency (Γ). Especially in late summer and fall the values are very small, with minima in October where all QFPs except QFP 5 assume Γ values that are at least another order of magnitude less than in the other months. The upper panel shows the corresponding NINO3 values. They are distributed symmetrically about zero, with QFPs 1 and 2 being negative and QFPs 4 and 5 being positive.

Figure 3 displays the outcome of the search algorithm. All Γ values are well below 0.3 (see lower panel), and especially the negative QFPs (1 and 2) are practically 0 for most months. Compared to Fig. 2 one sees that these numbers are significantly below the average value of $\hat{\Gamma}$. The numbers certainly suffer from some residual convergence failures of the search algorithm; this is especially clear for the spring and fall estimates of QFP 1 and QFP 2. The diagram reflects the fact that the flatness of the function $\Gamma(x)$ is directly related to the smallness of $|\partial\Gamma/\partial x|$ (middle panel) and, hence, to the difficulty in finding the correct minimum. In the upper panel we show the corresponding NINO3 values for the different months as calculated from the QFP. Already from the NINO3 values we see a symmetric behavior about the origin. This can be verified by inspecting the various fields corresponding to the QFPs. We show QFP 1 and QFP 5 of July in Fig. 4 in the fields SST, TCL, and wind (QFP 2 and QFP 4 are very similar to QFP 1 and QFP 5, respectively, with smaller amplitude). For QFP 1 (Fig. 4a) we see a tongue of negative SST anomalies (up to $-3.5°$) spreading from the South American coast, accompanied by a strong divergence in the wind field and a rather weak TCL field. The west Pacific shows a similar but smaller pattern in the SST and wind field, with reversed sign. In QFP 5 we observe the same pattern with reversed signs but note that the shifted ITCZ forces the wind field to converge or diverge at about 5°N. Note the splitting in two cells of the warm anomaly in the east Pacific.

To verify our findings we performed test runs of ZC_7 in the following way. We chose, for each QFP, 20 initial states that were random perturbations of that QFP with covariance $0.01C_9$ and ran the model 500 time steps, about 14 years. Figure 5 shows the result in the form of a phase plot between the two dominant PCs. The linearity of the dynamics can be read directly from these scatterplots since such a behavior appears as a circle or arc of the trajectory (when an oscillation is

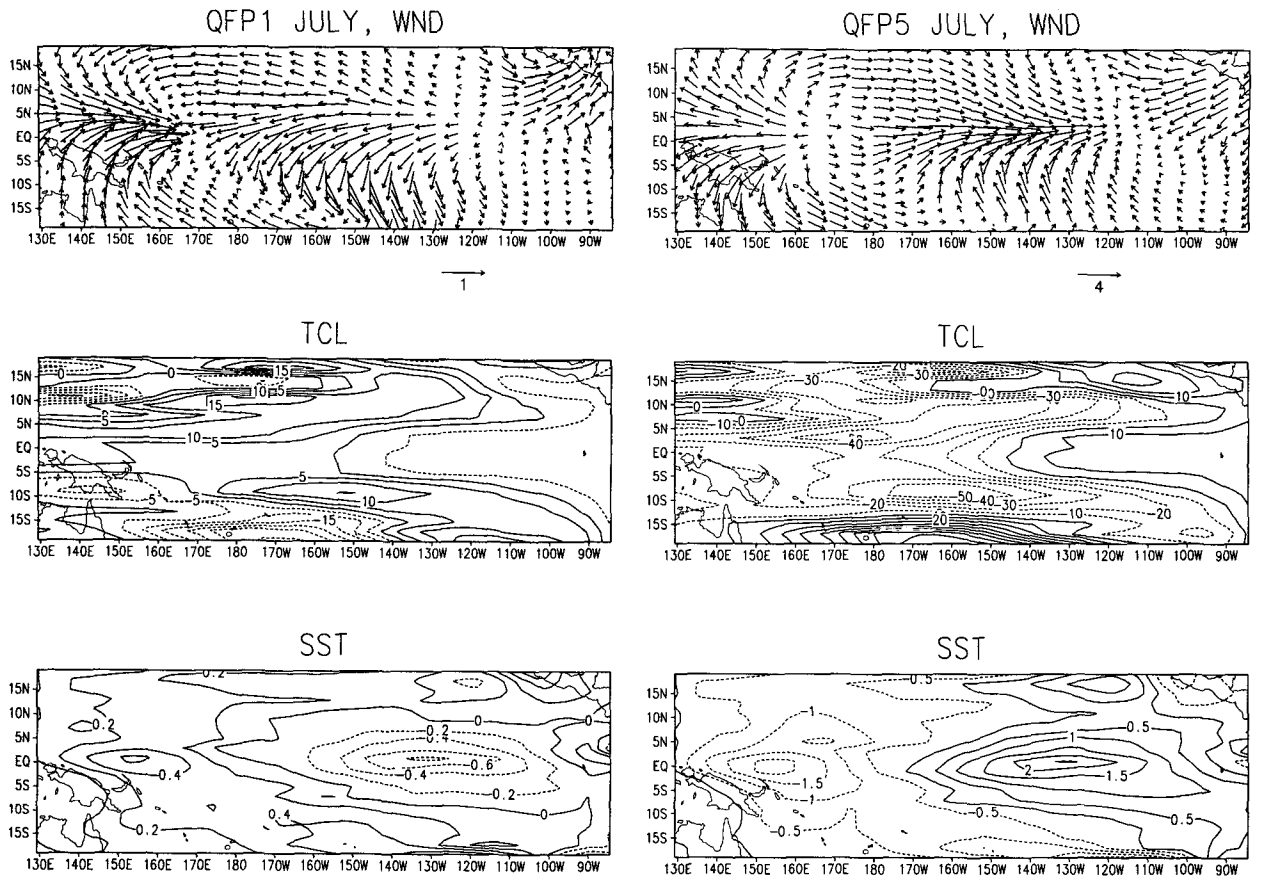

FIG. 4. (a) The wind, TCL, and SST fields of QFP 1 for the month of July. We see a cell of colder than normal (~−0.6°) temperatures in the eastern Pacific, accompanied by an upwelling Kelvin wave in the east and downwelling Rossby waves in the central Pacific. The wind field shows easterlies (~1 m s) in the central Pacific and stronger westerlies in the west, with a large convergence zone at about 165°E. This corresponds to a warm pool of surface water at 155°E. (b) Like (a) but for QFP 5. We mainly see a mirrored picture from the former figure, with opposite signs and enlarged amplitudes.

prevailing) or as a straight line in case it is a pure damping or amplification. The outcome for QFP 3 shows the behavior of a full fixed point. We can see very clearly an unstable oscillation between PCs 1 and 2. The rotation time is slightly greater than 4 years, which is about the internal ZC_7 period that is known from other studies (see Zebiak and Cane 1987). The amount of scattering here is a direct measure for the state's sensitivity to initial conditions or its internal error growth. Compared to, say, QFP 2 we observe a much larger scattering for QFP 3. For QFP 2 we can distinguish three bandlike structures. Each band represents a trace of the cloud of initial conditions, and the cloud is still glued together even after three rotations have been performed. This points to an enhanced predictability of the model when initialized from QFP 2. The behavior is quite similar for QFP 5, again with three bands clearly visible. The occurrence of three cycles in 14 years again establishes a periodicity of 14/3 ~ 4.3 years. For QFP 1 we again have the enhanced scatter of the evolution like for QFP 3, as well as the quasi-linear evolution (circles) observed there.

Another striking feature can be observed in the QFP 1 scatterplot: some trajectories circle back into the origin, indicating the existence of a stable manifold that comes from a fixed point of ZC_7 near QFP 1. In fact, if we let the model run further, it settles into an equilibrium that we show in Fig. 6. The equilibrium is characterized by cold anomalies in the entire Eastern Pacific and a warm spot on the equator at 170°W. This is accompanied by a deepened thermocline in the west, off the equator, and easterly winds east of it. We also see strong winds in the northeastern (northeasterlies) and southeastern corner (westerlies) of the basin. The fact that this equilibrium is not detected by our routine indicates that basic elements of its structure lie outside the nine-EOF space. The behavior of QFP 4 is quite similar to that of QFP 3, so that one might argue that QFP 4 is essentially QFP 3, with minor modifications induced by an incomplete estimation. On the other hand, the estimation procedure that often enough slipped into the track of QFP 3 in some cases detected QFP 4.

The existence and structure of the so found QFPs certainly depends on the number of retained EOFs. It

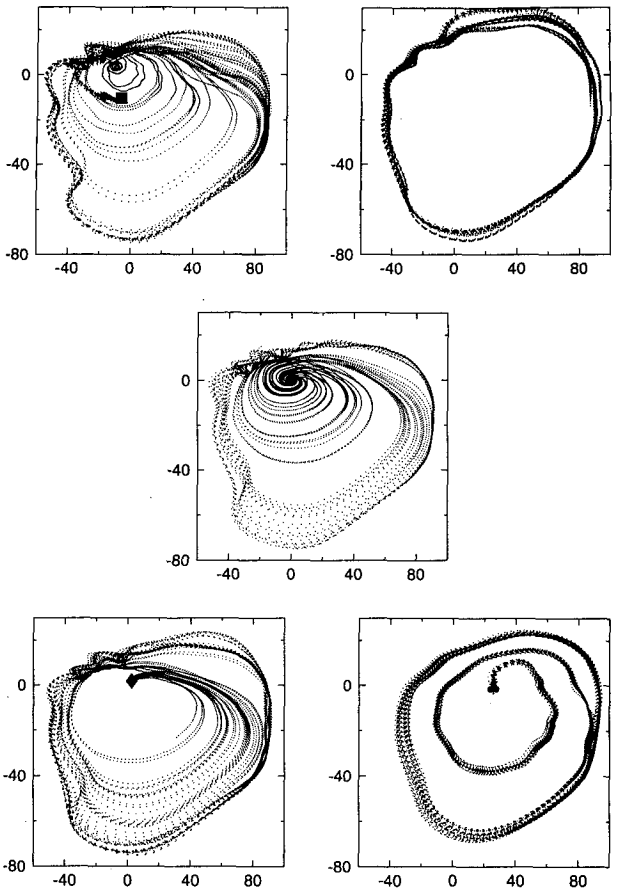

FIG. 5. Scatterplots of 20 ZC_7 runs started near each QFP, as reflected by the PC1 and PC2 components. The cloudiness of the evolution indicates strong error growth due to larger Lyapunov exponents. For QFP 1 (upper-left panel) one trajectory circles back into the origin, indicating a real fixed point near QFP 1 (see text). For QFP 2 (upper-right panel) the scatter is much less now, indicating enhanced stability. Note the great regularity for QFP 3 (middle panel). The circles indicate a prevailing unstable oscillation about QFP 3 (about 4 years per cycle). The QFP 4 behavior (lower-left panel) looks very similar to that of QFP 3. The QFP 5 scatter (lower-right panel) exhibits a quite stable rotation band, again with period of about 4 years. The scatter is very low, indicating strong stability.

appeared, however, that parallel experiments with 7, 8, 10, and 11 EOFs did not change the picture significantly. We also undertook similar experiments with 40 EOFs, which explain 99% of the variance. The results we gained so far indicate that the same structure of QFPs—the zero state and two pairs of patterns symmetrically about it—is still prevailing in this case. Moreover, the Γ values of many QFPs actually approach zero, so that one can deal with real fixed points. However, the computational resources needed for the detection and, especially, for the Kalman filter application are immense. Although the results look quite promising in some cases, we decided to stick to the lower-dimensional case, mainly because we prefered a broad overview over many parameter situations, which is possible for nine EOFs, to a sketch of one or two examples.

5. The local structure around the QFPs

The evolution of the error model in Kalman filtering is governed by the local linear structure of the model M_m. For the interactive Kalman filter we only need to know the localizations, that is, the Jacobian, at the single QFPs. A standard way to calculate the Jacobian at a state x is to advance the model M_m from, in our case, a set of nine perturbations of x, each of which points toward another unit vector. The solution matrix $\mathbf{L}_x$ can then be read from the so advanced unit-perturbations. We illustrate this by the following diagram:

$$x + \epsilon \mathbf{I} \xrightarrow{M_m} \epsilon \mathbf{L}_x. \tag{5}$$

The size of the perturbation ϵ was taken to be the 1% of the average variability as determined by C_9. As a comparison we estimated an average linearization $\mathbf{L}_m$ for each single month. We did this by advancing the model under fixed conditions for that month from a random set of initial conditions, with the covariance being C_9. The estimations were done by standard least squares techniques (see von Storch et al. 1988). As has been pointed out in BC for the evolution of any error model, the most stable and unstable modes of $\mathbf{L}_x$ or $\mathbf{L}_m$ are of central importance. We show these values in monthly diagrams in Fig. 7. The scale of the eigenvalues is given in e-folding times in months, where a negative time points to a stable and a positive time to an unstable eigenvalue. It is apparent that a major part of the variation is due to seasonality. For instance, the greatest instability is reached in the spring months where all eigenvalues cluster about 3–5-month e-folding time, whereas in late fall all instability seems to be gone (smallest e-folding time beyond 20 months). On the other hand there is also a widening of the spectrum of eigenvalues due to the internal dynamics, that is, coming from different QFPs. There are, for instance, significant differences in the behavior of some QFPs and the average model $\mathbf{L}_m$ in each single month. For example, in January QFP 1's most unstable mode e-folds in about 7 months, and QFP 5 in 17 months, whereas the strongest instability of $\mathbf{L}_m$ e-folds in 13 months. Furthermore, in November the only significant instability (8 months) comes from QFP 1. As for the most stable modes, differences also appear during certain months. In March one observes the most stable mode (from QFP 4) to be about 6.5 months, while the average model is not that stable (9 months); in June QFP 1 has a much more stable mode than the average model (5.5 months compared to 9 months). It is interesting that in all cases the average model shows the same stability properties as QFP 3, the state of no anomalies. All values for the average model are in good agreement with the findings of Xue et al. (1994). Some inconsistencies in the QFP values, such as the sudden

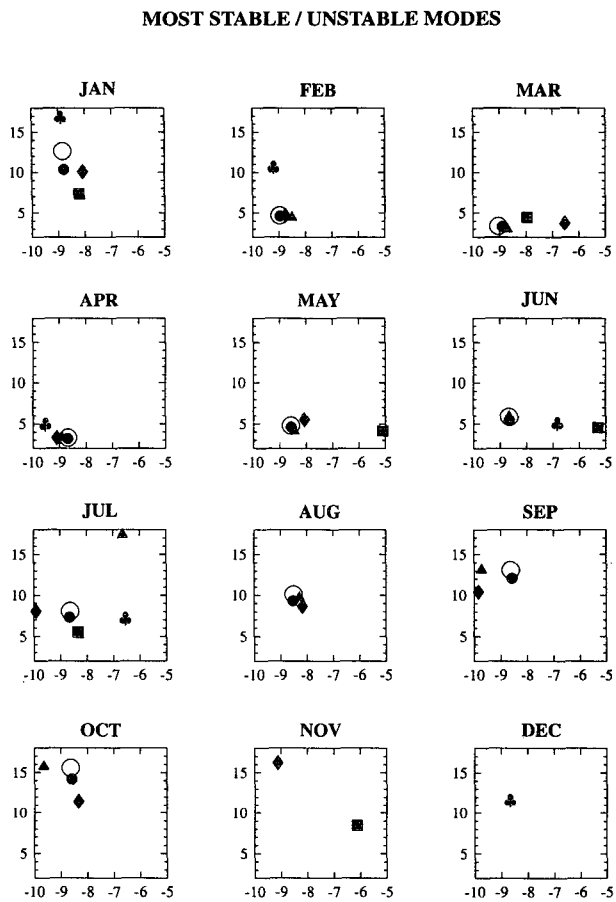

FIG. 6. The stability structure of the QFPs and the average linear model through the year. Values are e-folding times, negative values correspond to stable and positive to unstable modes. Here x axis is the most stable mode; y axis is the most unstable mode. We see a clear seasonal cycle, the instabilities being strongest in spring. The average model has only indifferent modes (eigenvalues approximately 1) in late fall, whereas QFP 1, for example, remains strongly stable in November. In the spring months the QFPs maintain a spectrum of different stability characteristics, such as QFP 4 in March, with a decay rate of 6.5 months and QFP 2 with 9 months (like the average model). The most unstable modes in springtime are similar between the average model and the QFPs (3 months in spring and over 20 months in late fall), but there are differences in the other parts of the year, like in January when QFP 1's most unstable mode e-folds in 7 months compared to 13 months for the average model. Note that the average linear model behaves quite like QFP 3, the linearization about the origin.

appearance of QFP 1 in November, are probably caused by errors in the QFP estimation. The general picture, however, seems sensible. It is hard to decide which kind of stability variation has a greater impact on a possible error model: the external seasonality or the internal dynamics coming from the different QFPs. This will have to be decided by running concrete assimilations.

Our stability analysis revealed one other thing that is interesting in its own right: for all months the second or third most unstable mode of QFP 3 (the zero state) was a complex mode with an e-folding time varying about 30 months and a period of almost exactly 2 years. Although we have dealt with the monthly models ZC_m, it is possible that this biennial mode is in essence the one that has been found in a number of observational studies, for example, Rasmusson et al. (1990), Barnett (1991), and Kepenne and Ghil (1992).

6. Seasonal, interactive, and extended Kalman filtering for ZC

In our final experiment we performed assimilations with three sorts of Kalman filters, where each filter used a specific method for the error model update. The assimilations were done in the following way. All processes under consideration are defined in the EOF reduced phase space. The *true* process was created by running the model ZC over a period of 100 years and projecting the result into the EOF space. The *observed* process was created by superimposing white noise on the true process that had the same spatial covariance as the true process times, some scaling factor ψ, which varied between 0 and 1; observations were made available once a month, that is, each third time step. We therefore have an exact knowledge of the observational error covariance. Our *model* of the true process is given by the model functions M_m for each month m. The Kalman filter is now well defined once we give it as input the observational error covariance R_t and the system error covariance Q_t (see the appendix). Both are taken to be constant. The former is determined by the white noise process, and the latter is estimated from another test run of 100 years. We calculated the actual errors between the next projected and the M_m forecast values of that run (these are different because of the EOF filtering). The three error models were 1) a *seasonal* model that used the monthly linearizations $\mathbb{L}_m$, 2) the *interactive* filter model, and 3) the full extended filter model. For the latter, we estimated the local Jacobian at each assimilation step by the same procedure as described in the former section.

From BC we adopt the notion of *regime* and *regime weight*. Given a (nonlinear) system s and a number N of states of s together with Jacobians, $(\omega_i, \mathbb{L}_i, i \leq N)$, they assign to each state of sN numbers $(\beta_i, i \leq N)$ with the following properties:

- $0 \leq \beta_i \leq 1$,
- $\Sigma\, \beta_i = 1$,
- $\omega_i, \mathbb{L}_i$ good approximation for $s \Rightarrow \beta_i \to 1$.

For details refer to the appendix. The name regime is inspired from situations when one of the β_i has very large values over a longer time span; it means that the system is nearly locked to the local linear system of the corresponding state.

A typical section of the IKF-assimilated ZC run, as seen by the regime weights, is depicted in Fig. 8; here we used an observational error scale of $\psi = 0.6$. We see the five weights (on top of each other) evolving

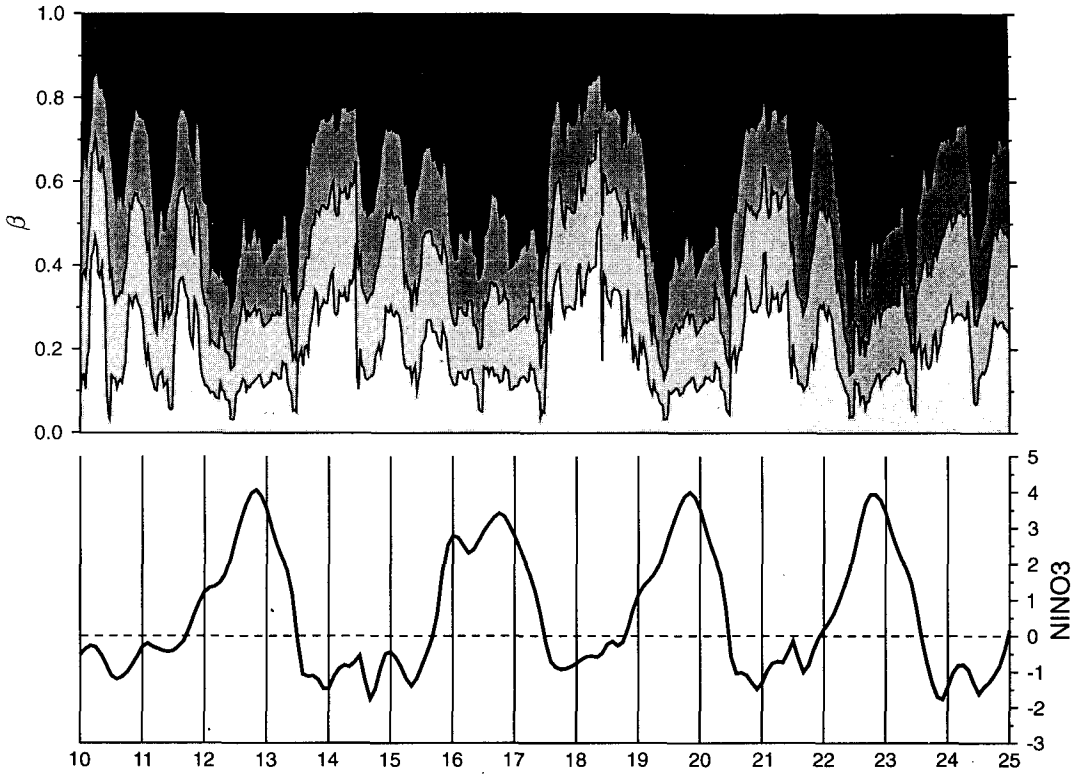

FIG. 7. A model run of ZC together with the QFP weights as used for the interactive Kalman filter (see text). The weights are depicted cumulatively, from bottom (β_1) to top (β_5), with increasing gray shades. We see the irregular periodicity in the weights (upper panel) that correspond to the behavior of NINO3 (lower panel). Note the strong El Niño events that are reflected in β_5; it seems that they are accompanied by two peaks in β_5 marking the onset and breakdown of an event. For La Niña events we see a large β_5 weight. The asymmetry between cold and warm phases usually encountered in ZC appears reduced in the regime weights.

synchronously with the current state of the system as measured by the NINO3 index. The largest weights are those of the extreme states, that is, QFP 1 and QFP 5. Most of the time the other QFPs show a rather parallel behavior with small weights, and one cannot distinguish (at least not from NINO3 alone) a specific situation that is linked to exactly one of them and that would justify the name, say, QFP 2 regime. This is different for QFP 1 and QFP 5: for QFP 5, we see that its weight is strongest, sometimes with $\beta_5 \geq 0.5$, during model El Niño events (like those of years 3, 10, and 13). Note that each warm event has two maxima at the beginning and the end. This could mean that for the creation and ending of an event, the stabilities and instabilities of QFP 5 are of great importance. For QFP 1, which reflects La Niña events, we note that while in NINO3 an event does not appear to be very pronounced, this is different for β_1. We see strong weights of QFP 1 of about 0.4 in years 14, 18, and 21. Generally, the well-known asymmetry in ZC between cold and warm phases does not show in the weights.

In Figure 8 we depict the outcome of the three assimilations: the assimilation error, the sensitivity (see the appendix), and the (true) NINO3. The most prominent signal we observe is the seasonal cycle in the sensitivity function. This is caused by the increased instability of the linear error models in springtime (cf. Fig. 6). The EKF sensitivity naturally shows a wider range of behavior, especially when a warm event breaks down and turns into a cold phase. Here the EKF sensitivity is consistently reduced, which means that during those times the filter tends to ignore observational input. Seemingly this is needed, however, since the assimilation error grows drastically during such breakdowns; a fact that is most likely due to the fast, switchlike changes of the system state at those times. This phenomenon is very similar to the one we observed in BC with the Lorenz system. Here the EKF was, under certain circumstances, unable to trace the switches that pushed the system from one quasilinear regime to the other.

This is different for both the seasonal filter and the IKF. Here we see a sensitivity that is practically independent of the ENSO cycle. To understand why the IKF performs better than the other filters we have to look at the average sensitivity. It is much higher for the IKF, a fact that is very likely caused by the enhanced instabilities in the QFP regimes (see Fig. 6 for com-

parison). It is still surprising, though, how little impact the current system state has on the IKF sensitivity (apart from the seasonal cycle). The larger influence of the observational input is crucial for the seasonal filter's and the IKF's capability to trace the breakdowns of an El Niño. But at least for the IKF this also applies to the general situation of a fast system change. In summer/fall of the years 12, 15, 22, for example, we observe smaller IKF assimilation errors when a warming happens rather rapidly. Likewise, the double event of year 16 is traced better by the IKF. The overall performance of the assimilation can be measured by the index Δ defined in the appendix; Δ is a measure of how much the observational error is reduced by the assimilation. Table 2 shows the outcome of each filter with five different levels ψ of observational noise.

The table shows that for smaller observational error noise (ψ = 0.2–0.6) the IKF performs best. The fact that all filters work suboptimal (with $\Delta > 100\%$) in some cases is caused by the unavailability of observations during two-thirds of the time. This could probably be remedied by increasing the system error, as has been shown by Miller and Ghil (1994) or also BC; but this goes beyond the topic of our study. The seasonal filter has the best performance for ψ = 1.0, but this error level might already lie in the realm where the performance just depends on the relative sizes of the variances of the true, the observed, and the model process.

TABLE 2. Kalman filter performance (assimilation error).

Δ (%)	Seasonal	IKF	EKF
0.2	170.4	143.0	171.1
0.4	107.5	94.4	109.3
0.6	76.0	70.7	78.6
0.8	58.1	58.0	61.5
1.0	46.9	50.4	50.3

7. Conclusions

The study just presented is the second step of three that tries to define and utilize, for the general context of data assimilation, the tendency of nonlinear systems

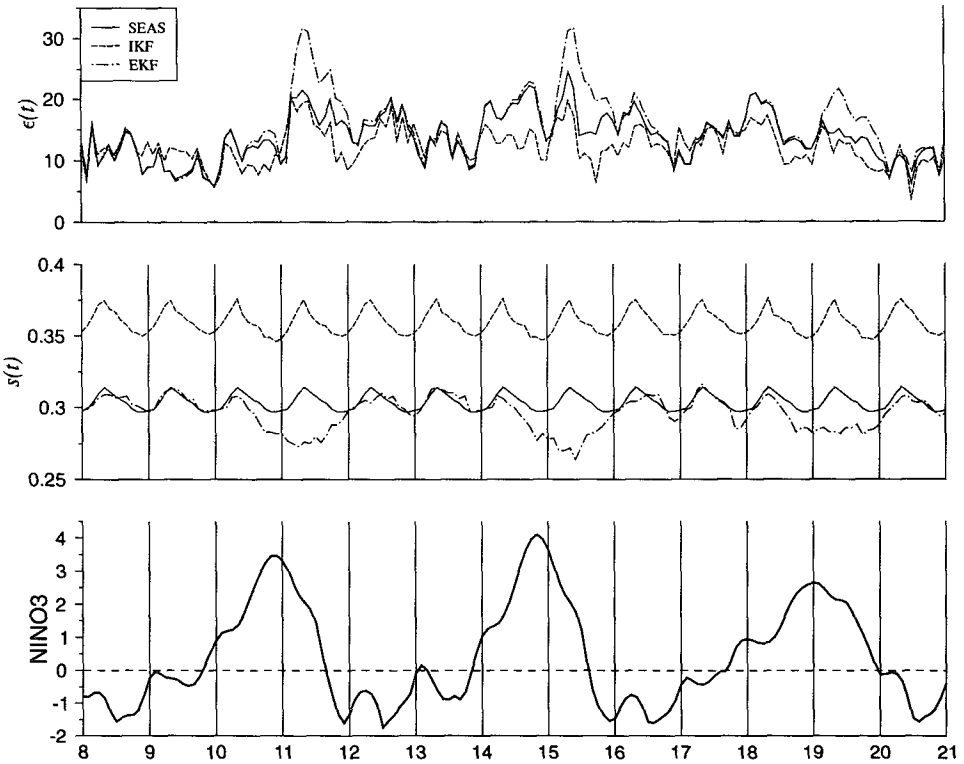

FIG. 8. The performance of the three assimilations using the seasonal (dashed lines), interactive (solid lines), and extended Kalman filter (dotted lines). During large El Niño events (lower panel), the assimilation error (upper panel) is markedly increased for the EKF. This is accompanied by a reduced sensitivity toward observations (middle panel). The sole variability in the seasonal model comes through the annual cycle, with larger sensitivity in spring and smaller in fall. The otherwise constant behavior ensures that the errors in tracking an El Niño breakdown are significantly reduced. The IKF sensitivity is significantly larger than that of the other two filters. This enables the IKF to trace all fast system changes better, not only the breakdowns but also the strong feedback mechanisms that lead to the onset of El Niño (like in summer/fall of years 12, 13, and 22). Moreover, the double event in year 16 is traced much closer.

to *form regimes*. Here we use the phrase "regime" in a slightly broader sense than usual, including regimelike behavior of the localizations of the respective models. The first step was the introduction and testing of the interactive Kalman filter. Crucial to the method is an a priori knowledge of the regimes that, for autonomous systems, can be identified with the fixed points and corresponding Jacobians of the system. For the testing we had used low-dimensional, highly nonlinear dynamical systems that could be treated purely algebraically as far as fixed points and Jacobians were concerned. Because the situation changes quickly as the dimension of the problem increases, we had to find other ways to detect fixed points and alternatives for the notion of fixed point itself. In this study we presented one natural generalization of that notion, the quasi-fixed point. By working in a reduced space one is able to define QFPs for a system as large as the Zebiak–Cane model ZC. A major theoretical difficulty is the question of how to reconcile the autonomous concept of QFP with the nonautonomous character of ZC. We attempted to achieve this by cutting ZC into autonomous monthly pieces ZC_m and find monthly QFPs for them. Although QFPs might, from a theoretical standpoint, suffer from deficiencies such as lack of uniqueness (their exact shape depends on the actual reduction), they still promise to be a valuable tool for data assimilation with the interactive Kalman filter.

The definition of a QFP is very simple: while the tendency of a system is zero for a fixed point, it is at a local minimum for a quasi-fixed point. Characteristic for fixed points and, depending on the value of the minimum, for QFPs is that the local structure about such a state is richest and therefore shows the largest variety of different stability–instability structures. A QFP can be determined by applying simple search routines that minimize a multidimensional real positive function, but not without some previous reduction of the system space in order to make it feasible. Since the reduced space had to contain all crucial initialization variables for ZC, we were led to apply a multiple-EOF reduction.

We kept nine multiple EOFs that explain about 90% of the full variance. By using a number of random states as first guesses for each month we found, after a cascade of further filtering and cleaning, five QFPs, QFPs, 1–5, that existed throughout the year, with slight variations in each month. The picture of the five QFPs looks rather symmetric. There are two cold states (QFPs 1 and 2) with an associated NINO3 value of about −0.4 and −0.1, and two warm states (QFPs 4 and 5) with NINO3 values of about 0.1 and 1.5, all of which have a similar pattern. The other QFP, QFP 3, is the state of no anomalies and it is a fixed point in the full model. The system's tendency at the QFPs is at least one to two orders of magnitude less than the average tendency. Similar EOF reductions, like when we retained 7, 8, 10, or 11 instead of nine EOFs, led to QFPs that resembled QFPs 1–5 very much. First experiments with 40 instead of nine EOFs indicate that the basic structure of the QFPs—two pairs of patterns symmetrically about the zero state—is inherited, and the "quality" of the QFPs is even improved as the states appear much closer to real fixed points. However, for a comprehensive overview one needs considerable amount of computing power, especially for the IKF applications.

As mentioned, the most important feature of the QFPs of the various ZC_m is their stability–instability structure, which is crucial for the Kalman filtering. We found that among the QFPs there is a broad spectrum of eigenvalues of the corresponding Jacobians, but the change of the season also affects the eigenvalue structure considerably. To demonstrate the usefulness of the QFPs, we performed a number of Kalman filtering experiments with the model ZC. Although this was done in a drastically reduced space, the general features are not unlike those encountered in a realistic setting where one assimilates real observational data into ZC. The results showed that the interactive filter performed better than both the seasonal as well as the extended Kalman filter. Although the major flexibility of all three filters is caused by the instabilities that vary through the seasonal cycle, the overall sensitivity is enlarged for the interactive filter. This result parallels the findings in our former experiments with low-dimensional highly nonlinear systems: that fast, switchlike changes of the system state can only be traced by an assimilation if the sensitivity toward observations is sufficiently high (but, of course, not too high). On the other hand, the results indicate that the fast changes in the ZC state and the corresponding error growth are in fact caused by strong nonlinearities, as opposed to, for instance, large singular vectors.

Practical as it might be, the use of stationary regimes like in the current study appears unappropriate for a model like ZC. Other models such as weather models of the extratropics with their typical regimelike behavior seem more promising. But here the problem of system reduction is cumbersome and computationally very expensive.

In Part II of our study we will assume a viewpoint that seems more appropriate for ZC. The nonautonomous nature of ZC will be accounted for by reinterpreting what we understood as a regime (in the broader sense). Instead of understanding it as one of a few characteristic monthly local behaviors, we come to view it as a locking of the full system evolution into one of a few possible orbits. This means we consider QFPs of an appropriate version of the Poincare map of ZC, which are nothing else than periodic orbits of ZC.

APPENDIX

The Interactive Kalman Filter

The basic equations for the interactive Kalman filter are as follows. We assume that the system, which is given by some model function f, approximately decomposes into N regimes $(\omega_i, \mathbf{L}_i)$, $i \leq N$. Here a regime

$(\omega, \mathbf{L})$ is given by some state ω of the system together with its Jacobian $\mathbf{L}$ at that state. By decomposition we mean that if we write the state vector at time $t-1$ as

$$x(t-1) = \omega_i + \xi_i(t-1), \tag{A1}$$

the forecast error of the regimes

$$\delta_i(t) = |f(\omega_i) + \mathbf{L}_i\xi_i(t-1) - f[x(t-1)]| \tag{A2}$$

should be comparatively small for at least one regime (here "| |" denotes the Euclidean norm in the phase space). This is reflected by the *weighting* of the regimes that assigns, at each time t of the process, to each regime $(\omega_i, \mathbf{L}_i)$, a number $\beta_i(t)$,

$$\beta_i(t) = \frac{1/\delta_i^2(t)}{\sum\limits_{j\leqslant N} 1/\delta_j^2(t)}, \tag{A3}$$

which is approaches 1 the better $(\omega_i, \mathbf{L}_i)$ approximates f. The assimilation step for the interactive Kalman filter goes as follows: Suppose we already assimilated data up to the time $t-1$. We therefore have calculated an assimilation value $\tilde{x}(t-1)$ and the error covariance $\mathbf{P}_{t-1}$, and from this we calculate the forecast value $\hat{x}(t) = f[\tilde{x}(t-1)]$. The independent observation gives us a value $\hat{x}(t)$. Now we calculate N (temporary) guesses of the forecast error covariance $\hat{\mathbf{P}}_t$ by using the respective regime models $\mathbf{L}_i$ and the system error covariance $\mathbf{Q}_t$, via

$$\hat{\mathbf{P}}^{(i)} = \mathbf{L}_i\mathbf{P}_{t-1}\mathbf{L}_i^{\mathrm{T}} + \mathbf{Q}_t. \tag{A4}$$

Now we can define the forecast assimilation error covariance $\mathbf{P}_t$ by

$$\hat{\mathbf{P}}_t = \sum_{i\leqslant N} \beta_i(t)\hat{\mathbf{P}}^{(i)}, \tag{A5a}$$

and, for the case that observations are available at time t, let

$$\mathbf{P}_t = (1 - \mathbf{K}_t)\hat{\mathbf{P}}_t(1 - \mathbf{K}_t)^{\mathrm{T}} + \mathbf{K}_t\mathbf{R}_t\mathbf{K}_t^{\mathrm{T}}, \tag{A5b}$$

with $\mathbf{K}_t$ denoting the Kalman gain matrix and $\mathbf{R}_t$ the observational noise covariance. Finally, the assimilated value is calculated by composing observational and model information, $\hat{x}(t)$ and $\hat{x}(t)$, by using the standard Kalman weighting

$$\tilde{x}(t) = (\mathbf{I} - \mathbf{K}_t)\hat{x}(t) + \mathbf{K}_t\hat{x}(t). \tag{A6}$$

Two quantities are of importance: the assimilation error

$$\epsilon(t) = |\tilde{x}(t) - x(t)| \tag{A7}$$

and the sensitivity of the assimilation toward observations

$$s(t) = \sum_{i\leqslant N}\left[\sum_{j\leqslant n}(\mathbf{K}_t)_{ij}^2\right]^{1/2}. \tag{A8}$$

A good performance index for the assimilation is the actual assimilation error covariance $\mathbf{P}$ relative to the observational noise, given by $\mathbf{R}$:

$$\Delta = \frac{\mathrm{Tr}(\mathbf{P})}{\mathrm{Tr}(\mathbf{R})}. \tag{A9}$$

REFERENCES

Barnett, T. P., 1991: The interaction of multiple time scales in the tropical climate system. *J. Climate,* **4,** 269–285.

Branstator, G., and J. D. Opsteegh, 1989: Free solutions of the barotropic vorticity equation. *J. Atmos. Sci.,* **46,** 1799–1814.

Bürger, G., and M. Cane, 1994: Interactive Kalman filtering. *J. Geophys. Res.,* **99,** (C4), 8015–8031.

——, S. E. Zebiak, and M. A. Cane, 1995: Quasi-fixed points and periodic orbits in the Zebiak–Cane ENSO model with applications in Kalman filtering. Part II: Periodic orbits. *Mon. Wea. Rev.,* **123,** 2814–2824.

Cane, M. A., S. E. Zebiak, and S. C. Dolan, 1986: Experimental forecasts of El Niño. *Nature,* **322,** 827–832.

Charney, J., and J. DeVore, 1979: Multiple flow equilibria in the atmosphere and blocking. *J. Atmos. Sci.,* **36,** 1205–1216.

Keppene, C., and M. Ghil, 1992: Adaptive filtering and the prediction of the Southern Oscillation index. *J. Geophys. Res.,* **97,** 20 449–20 454.

Latif, M., T. P. Barnett, M. A. Cane, M. Flügel, M. E. Graham, H. von Storch, J. S. Xu, and S. E. Zebiak, 1994: A review of ENSO prediction studies. *Climate Dyn.,* **9,** 167–179.

Legras, B., and M. Ghil, 1985: Persistent anomalies, blocking and variations in atmospheric predictability. *J. Atmos. Sci.,* **42,** 433–471.

Miller, R., M. Ghil, and F. Gauthier, 1994: Advanced data assimilation in strongly nonlinear dynamical systems. *J. Atmos. Sci.,* **51,** 1037–1056.

Preisendorfer, R. W., 1988: *Principal Component Analysis in Meteorology and Oceanography.* Elsevier, 324.

Press, W. H., S. A. Teukolsky, W. T. Vetterling, and B. P. Flannery, 1992: *Numerical Recipes in C.* Cambridge University Press, 994.

Rasmuson, E. M., X. Wang, and C. F. Ropelewski, 1990: The biennial component of ENSO variability. *J. Mar. Syst.,* **1,** 71–96.

von Storch, H., T. Bruns, I. Fischer–Bruns, and K. Hasselmann, 1988: Principal oscillation pattern analysis of the 30- to 60-day oscillation in a general circulation model equatorial atmosphere. *J. Geophys. Res.,* **93,** 11 022–11 036.

Xue, Y., M. A. Cane, S. E. Zebiak, and M. B. Blumenthal, 1994: On the prediction of ENSO: A study with a low order Markov model. *Tellus,* **46A,** 512–518.

Zebiak, S., and M. Cane, 1987: A model El Niño–Southern Oscillation. *Mon. Wea. Rev.,* **115,** 2262–2278.